



A data-driven comparative study of thermomechanical properties in rare-earth zirconate and tantalate oxides for thermal barrier coatings

Ying Zhang¹, William Yi Wang^{2,3,*}, Ke Ren⁴, Zhou Wang¹, Xingyu Gao⁵, Yiguang Wang⁴, Keke Zhang^{1,*}, Haifeng Song⁵, Xiubing Liang^{2,6}, Jinshan Li^{2,3,*}

Keywords:

Rare-earth oxides, fracture toughness, lattice thermal conductivity, key physical parameter, first-principles

Citation:

Zhang, Y.; Wang, W. Y.; Ren, K.; Wang, Z.; Gao, X.; Wang, Y.; Zhang, K.; Song, H.; Liang, X.; Li, J. A data-driven comparative study of thermomechanical properties in rare-earth zirconate and tantalate oxides for thermal barrier coatings. *J. Mater. Inf.* 2026, 6, 11.

<https://dx.doi.org/10.20517/jmi.2025.71>

Received: 14 Aug 2025

Accepted: 3 Sep 2025

Published: 2 Feb 2026

Academic Editor:

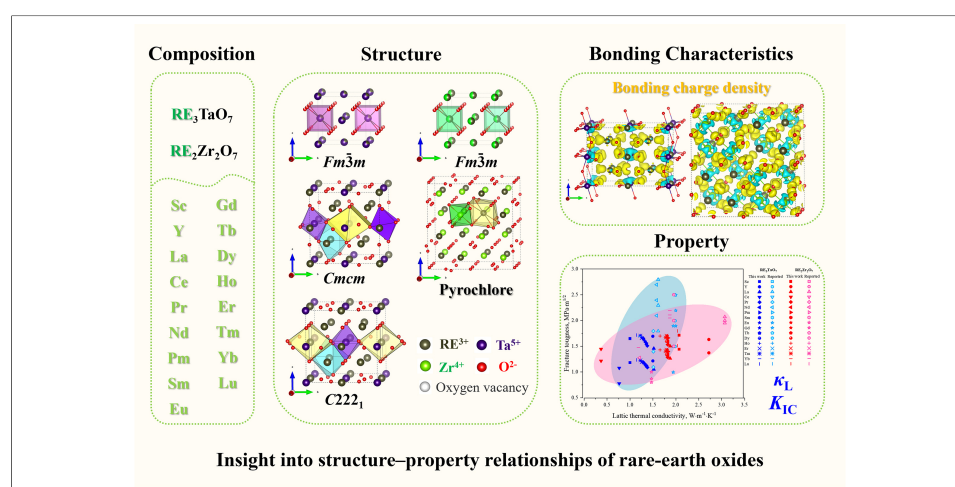
Zhiliang Zhang

Copy Editor:

Pei-Yun Wang

Production Editor:

Pei-Yun Wang



Abstract

Rare-earth (RE) zirconates and tantalates are promising candidates for next-generation thermal barrier coatings (TBCs) due to their high-temperature stability and low thermal conductivity. However, the substantial compositional complexity introduced by multiple RE element substitutions poses significant challenges for systematic property optimization. To address these challenges, a high-throughput, data-driven computational framework was employed to systematically investigate and compare structural stability, thermodynamic properties, lattice thermal conductivity (κ_L) and fracture toughness (K_{IC}) of RE₂Zr₂O₇ and RE₃TaO₇ oxides (RE = Sc, Y, La ~ Lu) in their pyrochlore and Weberite-type structures, respectively. κ_L and intrinsic K_{IC} were systematically evaluated using phonon-scattering and Griffith-based models. The results reveal that RE₃TaO₇ exhibits consistently lower κ_L than RE₂Zr₂O₇ due to its low symmetry, heavier atomic masses and higher structural disorder.

¹State Key Laboratory of Light Superalloys, Henan University of Science and Technology, Luoyang 471023, Henan, China.

²State Key Laboratory of Solidification Processing, Northwestern Polytechnical University, Xi'an 710072, Shaanxi, China.

³Innovation Center, NPU Chongqing, Chongqing 401135, China.

⁴Institute of Advanced Structure Technology, Beijing Institute of Technology, Beijing 100081, China.

⁵Laboratory of Computational Physics, Institute of Applied Physics and Computational Mathematics, Beijing 100088, China.

⁶Defense Innovation Institute, Academy of Military Sciences of the PLA of China, Beijing 100071, China.

*Correspondence to: Prof. William Yi Wang, Prof. Jinshan Li, State Key Laboratory of Solidification Processing, Northwestern Polytechnical University, Xi'an 710072, Shaanxi, China. E-mail: wywang@nwpu.edu.cn; ljsh@nwpu.edu.cn; Prof. KeKe Zhang, State Key Laboratory of Light Superalloys, Henan University of Science and Technology, Luoyang 471023, Henan, China. E-mail: zhkeke@haust.edu.cn

Interestingly, theoretical predictions indicate slightly higher intrinsic K_{IC} in $RE_2Zr_2O_7$, which is attributed to its ordered vacancy sublattice and symmetric bonding. In contrast, experimental data often report superior K_{IC} for RE_3TaO_7 , likely due to extrinsic microstructural effects not captured in idealized calculations. Correlation and SHapley Additive exPlanations analyses further reveal that bond energy, charge disorder and bond-length heterogeneity are key descriptors governing κ_L and K_{IC} . These findings provide mechanistic insight into structure–property relationships and offer a predictive framework for the rational design of RE oxide TBC materials.

Highlights

- Integrating high-throughput first-principles calculations, lattice-level descriptor engineering and interpretable machine learning to design $RE_2Zr_2O_7$ and RE_3TaO_7 (RE = Sc, Y, La ~ Lu) oxide-based thermal barrier materials.
- Data-driven selection and classification of key physical descriptors (bond energy, charge disorder, bond-length heterogeneity) enable predictive modeling of κ_L and K_{IC} across 17 rare-earth elements.
- Combining thermodynamic stability analysis, phonon-based transport models and SHapley Additive exPlanations interpretability to establish structure–property relationships and guide rational oxide design.

INTRODUCTION

Advancing the performance and reliability of thermal barrier coatings (TBCs) represents a persistent challenge in the development of next-generation high-temperature materials, particularly for demanding applications in aerospace propulsion and energy conversion systems^[1–3]. The continuous push toward higher operational temperatures and harsher service environments necessitates the discovery and design of ceramic materials that not only exhibit ultralow lattice thermal conductivity (κ_L) for efficient thermal insulation but also possess robust mechanical stability, exemplified by high fracture toughness (K_{IC}), along with enhanced resistance to environmental degradation^[4,5]. However, conventional yttria-stabilized zirconia (YSZ), currently the industry standard, faces intrinsic limitations above 1,473 K, primarily due to phase instability and accelerated degradation mechanisms^[6,7]. Consequently, exploring alternative ceramic systems with superior thermomechanical performance at elevated temperatures is of critical importance.

Rare-earth (RE)-based oxide ceramics, particularly RE zirconates and tantalates, have emerged as promising alternative candidates, owing to their intrinsically low thermal conductivity, high melting points, and exceptional structural stability at elevated temperatures^[8–12]. Furthermore, the compositional flexibility afforded by substituting and doping various RE elements enables precise tuning of lattice parameters and phonon scattering characteristics, significantly optimizing their thermal and mechanical properties. Recently, high-entropy oxides (HEOs), characterized by multicomponent RE element incorporation, have attracted considerable attention due to their unique capacity for simultaneously achieving ultralow thermal conductivity and enhanced K_{IC} , driven by severe lattice distortions and increased chemical disorder^[13–15]. Nevertheless, despite these promising attributes, the complexity introduced by a large compositional space and numerous potential element combinations presents a significant obstacle to systematic optimization. This complexity necessitates an efficient and systematic approach to elucidate the influence of each RE element on thermomechanical performance and to identify optimal compositions.

Recent studies have demonstrated that κ_L and K_{IC} of ceramic TBC materials are strongly influenced by atomic-scale structural characteristics, such as crystal lattice symmetry^[16–18], oxygen vacancy concentration^[19,20], local lattice distortion^[21–24], and the nature of chemical bonding^[25–27]. Reduced thermal conductivity is primarily achieved through enhanced phonon scattering mechanisms, typically arising from structural disorder, lattice anharmonicity, point defects, and atomic mass mismatch introduced via compositional complexity^[21,28–30]. For example, previous investigations demonstrated that structurally complex phases, such as defect fluorite and pyrochlore structures, effectively enhance phonon scattering,

thereby significantly reducing thermal conductivity^[29,31]. On the other hand, K_{IC} in ceramics predominantly depends on intrinsic factors, including bond strength, lattice rigidity, and phase stability, along with extrinsic toughening mechanisms such as crack deflection, bridging, and stress-induced phase transformations^[32–34]. Controlled introduction of structural distortions and interfaces is known to activate these toughening mechanisms, thereby improving fracture resistance in brittle oxide ceramics^[23,24,35]. Despite these advances, a comprehensive, systematic understanding of the individual contributions of different RE elements to the delicate balance between low κ_L and high K_{IC} in zirconate and tantalate systems remains elusive. Clarifying these relationships is essential for rationally optimizing and designing advanced TBC materials with tailored thermomechanical properties.

Traditional experimental approaches to thermal barrier material discovery, typically grounded in empirical trial-and-error methodologies^[36], face significant limitations when applied to the vast compositional space of RE oxides. The high cost, long cycle times and difficulty in isolating intrinsic structure–property relationships hinder the ability of these methods to identify high-performance candidates efficiently^[37–39]. Moreover, most existing studies focus on individual compositions, lacking a systematic cross-comparison of the full RE series. Addressing these challenges requires an integrated strategy that can both explore broad chemical design spaces and uncover the underlying physical principles governing thermomechanical performance^[40]. Advances in high-throughput computational methods combined with data-driven analyses have emerged as powerful tools for the accelerated discovery and rational design of complex, multicomponent materials^[3,41,42]. By systematically computing material properties across broad chemical spaces using first-principles calculations and subsequently analyzing the resulting large datasets, these approaches enable the identification of key physical parameters and governing principles that link atomic-scale features to macroscopic behavior^[43]. For instance, such approaches have identified correlations between ionic charge and thermal conductivity in perovskite oxides^[44] and quantified the impact of severe lattice distortion on K_{IC} in ceramics by linking it to local bonding environments and macroscopic elastic/plastic properties^[26,27]. In addition, they have revealed how atomic bonding distortions directly influence phonon scattering and reduce thermal conductivity in RE oxides^[13,27].

In this work, the present work systematically investigates and compares structural stability, κ_L , K_{IC} , and bonding characteristics in $RE_2Zr_2O_7$ (pyrochlore/defect fluorite) and RE_3TaO_7 (Weberite-type/defect fluorite) oxides across 17 RE elements (RE = Sc, Y, La ~ Lu). Although RE_3TaO_7 and $RE_2Zr_2O_7$ oxides differ in stoichiometry and crystal symmetry, both systems feature BO_6 (B = Ta or Zr) octahedra and distorted RE coordination polyhedra derived from fluorite-related frameworks. These structural analogies, together with shared controlling factors such as RE ionic radius ($r_{RE^{3+}}$), bond distortion and electronic distribution, support a unified structure–property comparison across both families. By employing a high-throughput calculations approach combined with data-driven analytics, this study generates an extensive dataset encompassing formation energy (E_{form}), equilibrium volume (V_0), lattice parameters, bond characteristics, thermal conductivities, and K_{IC} . Subsequent correlation analyses and dimensionality reduction techniques identify key atomic-scale descriptors, including ionic radius, bond-length heterogeneity and valence state stability, that critically govern thermomechanical properties. This study elucidates the fundamental mechanisms dictating the trade-offs between low thermal conductivity and high K_{IC} in these oxide families, thereby providing an essential data-driven foundation to guide the rational selection and design of next-generation TBC materials. Moreover, the methodological framework demonstrated herein exemplifies how data-driven approaches can significantly advance the fundamental understanding of structure–property relationships in complex multicomponent ceramic systems, aligning closely with current objectives in high-impact materials science research.

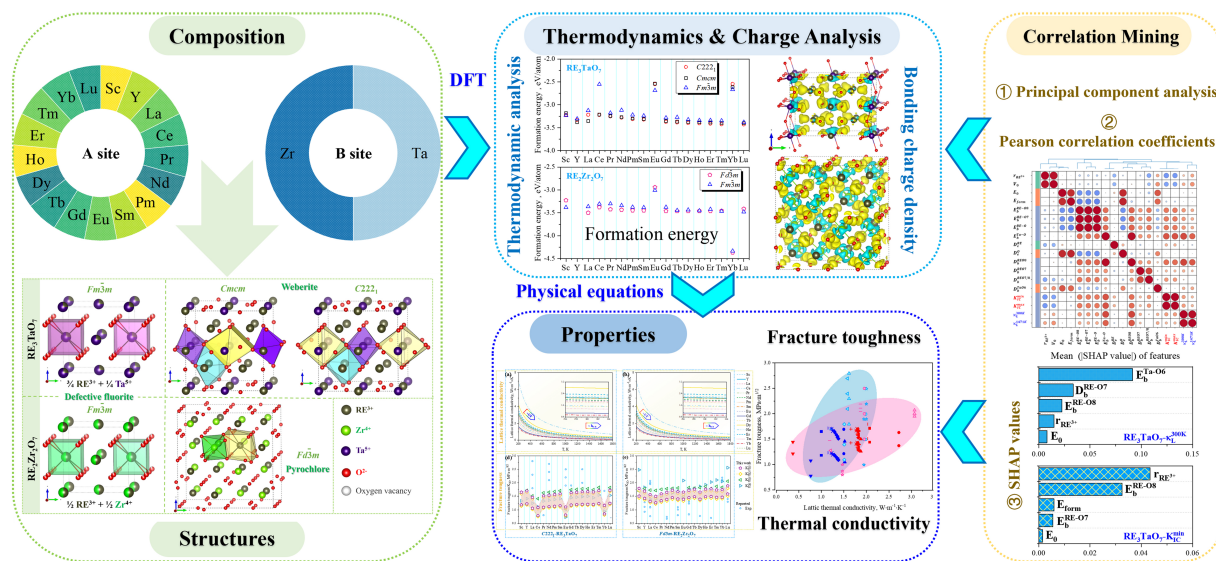


Figure 1. Schematic overview of the computational workflow for uncovering the structure–property relationships of the RE_3TaO_7 and $RE_2Zr_2O_7$ oxides.

MATERIALS AND METHODS

Computational workflow

A high-throughput computational workflow was employed to establish structure–property relationships in RE_3TaO_7 and $RE_2Zr_2O_7$ oxides, as shown in Figure 1. The workflow begins with compositional enumeration across 17 RE elements ($RE = Sc, Y, La \sim Lu$), followed by crystal structure selection based on predicted stable phases. Subsequently, density functional theory (DFT) calculations were performed to extract key thermodynamic and bonding descriptors. These data feed into property prediction models for K_{IC} and κ_L . Finally, data-driven analyses, including principal component analysis (PCA), Pearson correlation, and SHapley Additive exPlanations (SHAP)-based interpretability methods, were applied to systematically evaluate the influence of each descriptor on the predicted K_{IC} and κ_L . These analyses identify the most relevant features and provide both statistical and model-driven insight.

Crystal structure

The RE_3TaO_7 and $RE_2Zr_2O_7$ oxide families exhibit a rich diversity of crystal structures, each governed by the ionic radius of the RE ($r_{RE^{3+}}$) cation and the charge and size of the B-site cation (Ta^{5+} or Zr^{4+}). These structures can be categorized into ordered and disordered fluorite-derived frameworks, with representative models illustrated in Figure 1. In the RE_3TaO_7 system, three primary structure types are observed. The defect fluorite structure (space group $Fm\bar{3}m$) features a disordered arrangement of RE^{3+} and Ta^{5+} on the cation sublattice, with one-eighth of oxygen sites vacant for charge compensation^[11]. Larger RE^{3+} cations stabilize the $Cmcm$ phase, whereas medium-sized RE^{3+} elements favor the $C222_1$ structure, commonly referred to as the Weberite type. Both ordered structures exhibit distinct BO_6 octahedral frameworks and layered arrangements of oxygen vacancies, leading to pronounced structural anisotropy. In contrast, $RE_2Zr_2O_7$ compounds crystallize in either the defect fluorite ($Fm\bar{3}m$) or ordered pyrochlore ($Fd\bar{3}m$) structures, depending on RE^{3+} size^[45]. The pyrochlore phase features an ordered arrangement of RE and Zr on the A and B sublattices, respectively, with one-eighth of the anion sites vacant in a periodic fashion. Smaller RE^{3+} ions favor the defect fluorite phase, which exhibits full cationic disorder and randomly distributed oxygen vacancies. The transformation from ordered to disordered fluorite structures in both oxide families reflects the increasing ability of the lattice to accommodate strain as ionic radii decrease. Specifically, given the lack of experimental evidence for this compound, the results for $Sc_2Zr_2O_7$ and Sc_3TaO_7 are included for computational completeness only and should be interpreted with caution.

First-principles calculations

All DFT calculations were carried out using the projector augmented wave (PAW) method with the Perdew–Burke–Ernzerhof (PBE) exchange–correlation functional within the generalized gradient approximation (GGA) as implemented in the Vienna Ab initio Simulation Package (VASP)^[46]. Spin polarization was enabled, and the plane-wave energy cutoff was set to 1.4 times the maximum elemental ENMAX, where ENMAX denotes the recommended kinetic energy cutoff specified in the VASP pseudopotential files. k-point meshes of $4 \times 4 \times 4$ ensured convergence of total energy within 10^{-6} eV/atom⁻¹. Although applying Hubbard U corrections may improve prediction accuracy, the primary focus of this work is on trend-level comparisons across a wide compositional space. Several studies have established the effectiveness of GGA functionals in describing the properties of RE compounds^[47–49]. Therefore, omitting U corrections introduces negligible error in the context of structural, elastic, and thermodynamic analysis. Moreover, this choice avoids the element-specific arbitrariness associated with U parameter selection and ensures methodological consistency throughout the high-throughput workflow^[49]. Accordingly, all calculations in this study were carried out using the PBE functional within the GGA framework without +U corrections^[50], providing a robust and computationally efficient platform for capturing structure–property relationships in RE zirconates and tantalates. The V_0 and equilibrium energy (E_0) were obtained by fitting the total energy–volume data to the four-parameter Birch–Murnaghan equation of state^[51]. Elastic constants were obtained using the energy–strain method, from which mechanical properties including bulk modulus, shear modulus, Young’s modulus, and Poisson’s ratio were derived via the Voigt–Reuss–Hill averaging scheme^[52,53].

Lattice thermal conductivity

The thermodynamic combinatorial model is employed to predict the Debye temperature Θ , Grüneisen parameters γ to the temperature-dependent κ_L in oxides^[27]. Specifically,

$$\Theta = s(v)AV_0^{1/6} \left(\frac{B_0}{M_{av}} \right)^{1/2} \left(\frac{V_0}{V} \right)^\gamma, \gamma = \frac{1}{2} \left(\frac{dB}{dP} \right)_{T=0K} - \frac{1}{2}$$

have been selected as the best descriptors for calculating κ_L in the Slack equation:

$$\kappa_L = A \frac{M_{av} \Theta^3 V_0^{1/3}}{n^{2/3} T \gamma^2}$$

where A is a constant, M_{av} is average atomic mass, n denotes the number of atoms in the unit cell, V_0 represents the atomic volume. This formulation was applied to $\text{RE}_2\text{Zr}_2\text{O}_7$ and RE_3TaO_7 oxides with temperatures ranging from 200 to 1,800 K, as reported in Ref^[27].

The effective thermal conductivity κ_{eff} was normalized as

$$\kappa_{eff} = \kappa_L \left(1 - \frac{4}{3}\phi \right),$$

where the porosity ϕ is set to 5% in accordance with experiment^[54].

Fracture toughness

The Griffith Criterion is a foundational theory in fracture mechanics for brittle materials. It postulates that crack propagation occurs when the elastic strain energy released by crack extension is sufficient to overcome the energy required to create the new crack surfaces (surface energy, γ). K_{IC} is related to the Young’s modulus (E) and fracture energy ($G_c = 2\gamma$ for mode I fracture in brittle materials) through an expression of the form^[55,56]

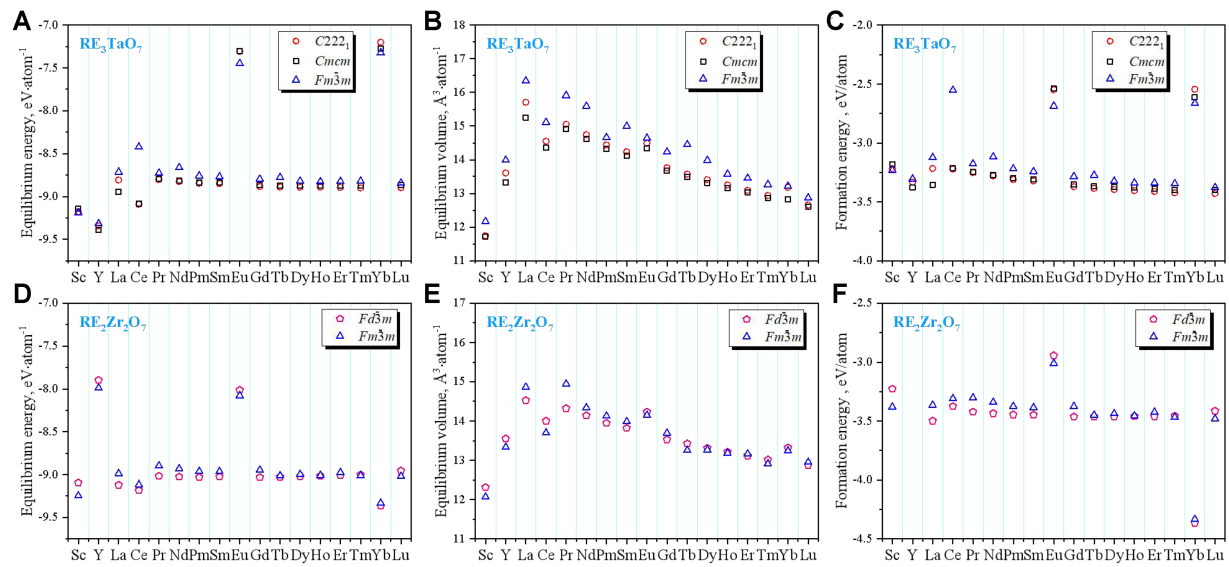


Figure 2. Thermodynamic analysis for (A–C) RE_3TaO_7 and (D–F) $\text{RE}_2\text{Zr}_2\text{O}_7$ comparisons (RE = Sc, Y, La ~ Lu), including (A and D) Equilibrium energy, (B and E) equilibrium volume and (C and F) formation energies of different phases. Symbols denote space groups: $C222_1$, $Cmcmm$ and $Fm\bar{3}m$ for RE_3TaO_7 ; $Fd\bar{3}m$ and $Fm\bar{3}m$ for $\text{RE}_2\text{Zr}_2\text{O}_7$ oxides. RE: Rare-earth.

$$K_{IC} = \sqrt{\frac{2E\gamma}{1-\nu^2}} \approx \sqrt{2E\gamma}$$

where ν is Poisson's ratio. Calculation details for the surface energy (γ) are provided in Ref.^[57]. It is important to note that Griffith theory generally predicts the fracture strength of materials containing pre-existing flaws, rather than the ideal theoretical strength of a perfect crystal. In practice, semi-empirical predictive models, derived from fitting experimental data, are often employed to provide correction factors for different material systems^[58,59].

RESULTS AND DISCUSSION

Structural stability and thermodynamic trends

The thermodynamic stability, V_0 , and E_0 of RE_3TaO_7 and $\text{RE}_2\text{Zr}_2\text{O}_7$ oxides are systematically evaluated across 17 RE elements (RE = Sc, Y, La ~ Lu) using first-principles calculations in the relevant crystal structures as illustrated in Figure 2. For the RE_3TaO_7 oxides, V_0 exhibits a consistent decreasing trend corresponding to the well-documented lanthanide contraction as the ionic radius of RE ions decreases. Among the investigated configurations, the orthorhombic $C222_1$ phase is thermodynamically most favorable for RE^{3+} cations of intermediate size (e.g., Sm ~ Dy, Y), while the $Cmcmm$ structure is stabilized by the largest cations (La, Pr). The disordered fluorite structure becomes energetically competitive for smaller RE ions due to its ability to accommodate local strain through enhanced structural flexibility^[60,61]. Similarly, the $\text{RE}_2\text{Zr}_2\text{O}_7$ oxides also demonstrate volume contraction consistent with decreasing $r_{\text{RE}^{3+}}$. However, these zirconates exhibit notably lower E_{form} compared to their tantalate counterparts, indicating superior intrinsic thermodynamic stability. In $\text{RE}_2\text{Zr}_2\text{O}_7$ oxides, an ordered pyrochlore structure ($Fd\bar{3}m$) is the most stable for larger RE ions, while a disordered fluorite structure is increasingly stabilized as the $r_{\text{RE}^{3+}}$ decreases, driven primarily by structural flexibility. Notably, the transition to disorder occurs at a larger ionic radius in $\text{RE}_2\text{Zr}_2\text{O}_7$ than in RE_3TaO_7 , underscoring the greater rigidity and lower defect tolerance of the Zr–O framework compared to Ta–O^[19].

To identify underlying correlations among structural and thermodynamic parameters, PCA was conducted using four standardized descriptors: $r_{\text{RE}^{3+}}$, E_0 , V_0 , and E_{form} . Given the heterogeneous physical dimensions of these features, z-score normalization was applied, and the correlation matrix was selected as the basis for

decomposition. For both RE_3TaO_7 and $\text{RE}_2\text{Zr}_2\text{O}_7$ systems, the first two principal components account for over 95% of the total variance, indicating that the dimensionality reduction retains the vast majority of structural–thermodynamic information. The loading patterns suggest that E_{form} and V_o contribute most strongly to the first principal component (PC1), whereas $r_{\text{RE}^{3+}}$ and E_o dominate the second component (PC2). This orthogonal separation implies that atomic packing (reflected by V_o) and chemical stability (reflected by E_{form}) capture complementary axes of variability across the RE series.

Thermal conductivity and fracture toughness

The high-temperature performance of $\text{RE}_2\text{Zr}_2\text{O}_7$ and RE_3TaO_7 oxides as TBCs is strongly governed by their κ_L and K_{IC} . In this study, κ_L and K_{IC} were systematically evaluated for the pyrochlore ($Fd\bar{3}m$) $\text{RE}_2\text{Zr}_2\text{O}_7$ and Weberite-type ($C222_1$) RE_3TaO_7 phases using a combined model for κ_L and the Griffith-based energetic model for K_{IC} . The adopted models for predicting κ_L and intrinsic K_{IC} have been previously validated by prior studies on HEOs^[27,62]. Specifically, the Debye–Slack formalism and its extensions have shown predictive accuracy within 15% when benchmarked against experimental κ_L for RE oxides, particularly those with well-defined phonon spectra and moderate anharmonicity^[27,44]. For K_{IC} , the Griffith-based energetic models employed here, especially the variant incorporating surface energy and Young’s modulus, are recognized as robust estimators for brittle systems, capturing relative trends and chemical effects despite neglecting extrinsic toughening mechanisms^[62]. These models provide a reliable basis for high-throughput screening, balancing physical realism with computational feasibility.

To ensure the validity of thermal conductivity predictions across the studied temperature range (200–1,800 K), potential structural phase transitions were carefully considered. For $\text{RE}_2\text{Zr}_2\text{O}_7$, a well-established order–disorder transition from the pyrochlore to defect-fluorite phase occurs at elevated temperatures, typically between 1,530 and 2,400 °C (1,803–2,673 K), depending on the $r_{\text{RE}^{3+}}$ ^[18]. Similarly, RE_3TaO_7 oxides are known to undergo a transition from the orthorhombic weberite-type ($C222_1$) structure to a disordered fluorite phase at temperatures generally above 1,973 K^[10,63]. These transition points lie beyond the temperature range considered in this work. Accordingly, all κ_L calculations were conducted using the most stable DFT-predicted phase at 0 K for each composition. The quasi-harmonic Debye–Grüneisen model employed here assumes a single, temperature-invariant phase and is therefore valid up to the onset of these high-temperature transitions. As no phase changes are expected within the modeled range (200–1,800 K), the resulting predictions reliably capture the intrinsic thermal transport behavior of the respective ground-state structures.

The calculated temperature-dependent κ_L from 200 to 1,800 K, incorporating 5% porosity corrections for representative oxides in both families is shown conceptually in Figure 3A and B. At lower temperatures, κ_L rapidly decreases following a typical inverse temperature dependence ($1/T$), governed by intrinsic phonon–phonon Umklapp scattering. At higher temperatures, κ_L approaches a minimum limit (κ_{min}) due to phonon mean free paths converging toward interatomic distances, indicative of pronounced phonon scattering. As shown in Figure 3C, RE_3TaO_7 consistently exhibits lower κ_L (0.76–1.52 $\text{W}\cdot\text{m}^{-1}\cdot\text{K}^{-1}$ at 300 K) compared to $\text{RE}_2\text{Zr}_2\text{O}_7$ (1.7–2.8 $\text{W}\cdot\text{m}^{-1}\cdot\text{K}^{-1}$ at 300 K), a trend maintained across the entire temperature range. The lower κ_L of RE_3TaO_7 oxides primarily results from their inherently lower symmetry ($C222_1$), greater structural complexity and consequently increased phonon scattering. Additional factors, including larger atomic mass differences and oxygen sublattice disorder, further reduce κ_L by intensifying phonon scattering channels.

For the identification of the optimal model for predicting K_{IC} , Figure 3D–F compares the results obtained from various models ($K_o^{(1)}$ and $K_o^{(2)}$ for energetic, $K_o^{(3)}$ and $K_o^{(4)}$ for empirical) for oxides, alongside the reported results. Among these models, $K_o^{(1)} = \sqrt{\frac{2E\gamma}{1-\nu^2}}$ ^[55] and $K_o^{(2)} = \sqrt{2E\gamma}$ ^[56] represent toughness estimates

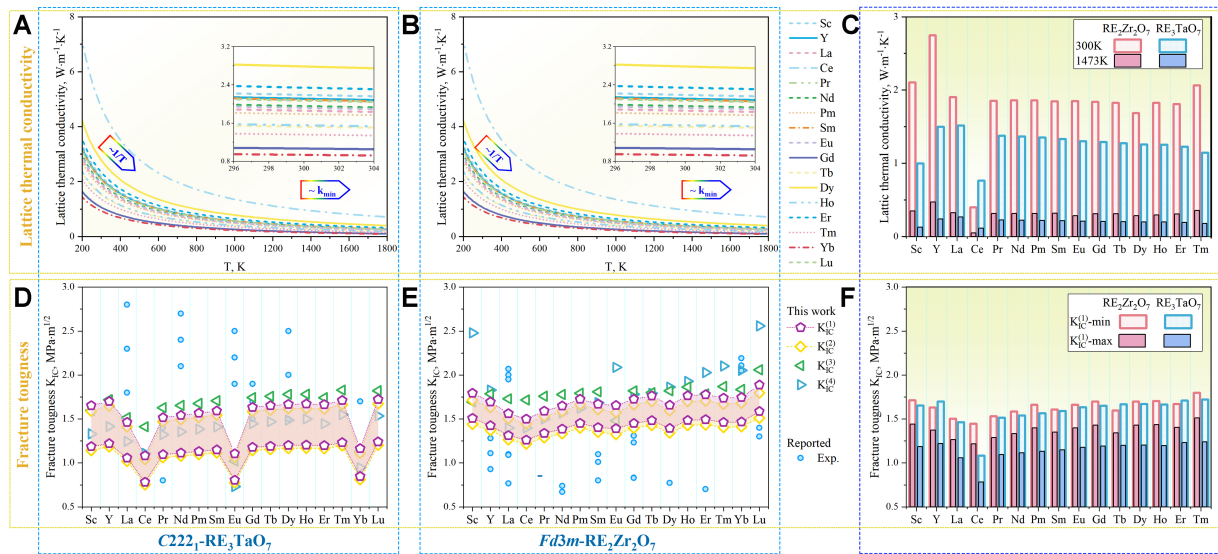


Figure 3. Temperature-dependent κ_L for (A) C222, RE₃TaO₇ and (B) RE₂Zr₂O₇ pyrochlore oxides by the combinatorial approach ($K_{IC}^{(n)}$) with 5% porosity correction; (C) κ_L values at 300 and 1473 K. Calculated K_{IC} by $K_0^{(n)}$ where $n = 1-4$ for (D) RE₃TaO₇ and (E) RE₂Zr₂O₇ oxides, together with the reported result^[69-80]; (F) Comparison of the minimum and maximum predicted K_{IC} values by $K_0^{(1)}$.

particularly suitable for brittle fracture systems. $K_0^{(3)} = (1 + \alpha) V_0^{1/6} G(B/G)^{1/2}$ [$\alpha = 0$] and $K_0^{(4)} = \alpha_0^{-1/2} V_0^{1/6} (\zeta(\nu) E)^{3/2}$ [$\alpha_0 = 8,840$ GPa], are empirical models that consider modulus ratios and bond characteristics and provide complementary insight into ionic and covalent contributions. The shaded regions represent K_{IC} limits calculated using the highest and lowest surface energy values for each structure. Through plotting surface energy (γ) as a function of relative orientation along planes [i.e., from (001) \rightarrow (012) \rightarrow (011) \rightarrow (021) \rightarrow (010)], the C222₁ and pyrochlore structures have the lowest γ with the most energetic favorable (031) and (110) surfaces, respectively. As shown in Figure 3D and E, K_{IC} increases with decreasing $r_{RE^{3+}}$ in both systems. Among the tested models, $K_0^{(1)}$ was selected for subsequent analysis due to its consistent performance and theoretical robustness. Intriguingly, the calculations predict that RE₂Zr₂O₇ generally exhibits slightly higher intrinsic K_{IC} (~ 1.80 MPa \cdot m^{1/2}) than RE₃TaO₇ (~ 1.6 MPa \cdot m^{1/2}), particularly for mid-sized RE ions. This is attributed to the highly ordered pyrochlore structure in RE₂Zr₂O₇, where periodic oxygen vacancy arrangements may enable crack deflection or microcrack formation, where mechanisms favorable for intrinsic toughening. However, this theoretical prediction contrasts with experimental observations, where RE₃TaO₇ often demonstrates higher or comparable K_{IC} (1.0–2.6 MPa \cdot m^{1/2})^[11] than RE₂Zr₂O₇. This discrepancy arises from the difference between intrinsic (defect-free) and extrinsic (microstructure-sensitive) K_{IC} . Theoretical models inherently exclude microstructural effects such as grain boundaries, porosity, domain switching and residual stress, which play a crucial role in experimental measurements.

Figure 3F summarizes these trends, highlighting that while RE₂Zr₂O₇ oxides demonstrate uniformly high intrinsic K_{IC} across the RE series, the C222₁-type RE₃TaO₇ oxides exhibit greater variability, with maximum toughness predicted for Tm₃TaO₇ and Lu₃TaO₇. The superior intrinsic performance of RE₂Zr₂O₇ is closely linked to its symmetric bonding network and ordered defect structure, which provide effective energy dissipation near crack tips^[64]. In contrast, the more complex and disordered lattice of RE₃TaO₇ limits such toughening routes under idealized conditions. Moreover, the combined plot of K_{IC} vs. κ_L at room temperature directly illustrates the inherent trade-off between mechanical robustness and thermal insulation, as shown in

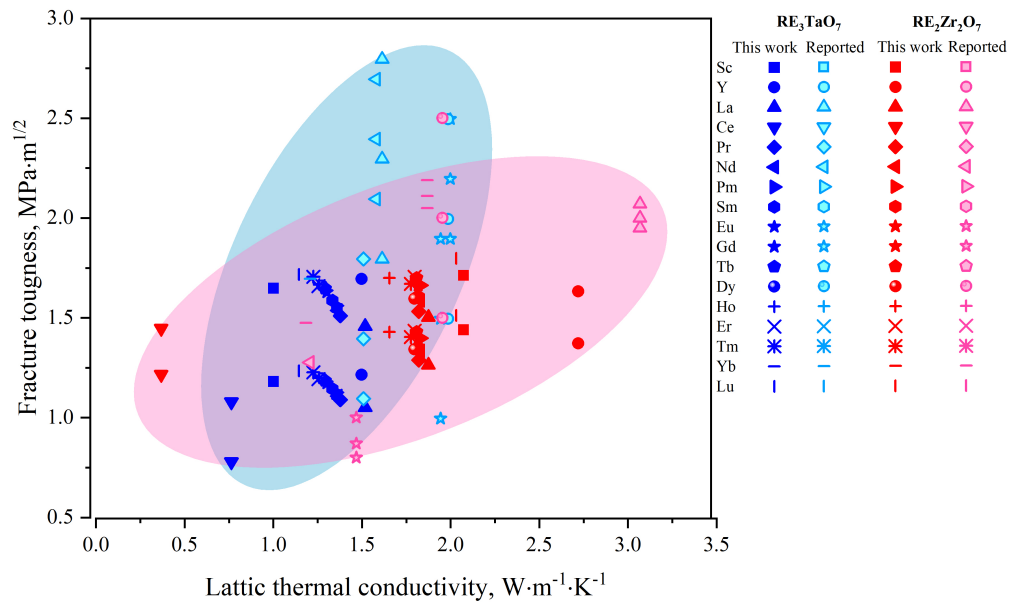


Figure 4. The relationship between lattice thermal conductivity at 300 K by and fracture toughness for RE_3TaO_7 and $\text{RE}_2\text{Zr}_2\text{O}_7$ with reported data^[10,76,81–83].

Figure 4. $\text{RE}_2\text{Zr}_2\text{O}_7$ oxides cluster within a region of high K_{IC} and moderate thermal conductivity, ideal for applications prioritizing mechanical integrity. In contrast, the orthorhombic $\text{C}222_1$ -type RE_3TaO_7 oxides occupy the low- κ_1 , moderate- K_{IC} region, which is advantageous for maximizing thermal insulation, albeit potentially at the expense of mechanical robustness. These results, validated against available experimental data, underscore the effectiveness of the data-driven predictive framework employed.

Atomic and electronic attributes of lattice distortion

To clarify the atomistic origins governing the thermal conductivity and K_{IC} of RE-based RE_3TaO_7 and $\text{RE}_2\text{Zr}_2\text{O}_7$ oxides, detailed analyses of bonding environments were conducted. These include bonding charge density distributions and quantitative descriptors related to bond length and charge heterogeneity. Such atomic-scale characterizations directly inform the macroscopic property trends observed, offering a unified descriptor-based framework justified by the structural similarities between the two oxide families - both composed of interconnected BO_6 octahedra ($\text{B} = \text{Ta}$ or Zr) and distorted RE–O polyhedra, despite differences in nominal RE:O ratios.

As shown in **Figure 5**, bonding charge density ($\Delta\rho$)^[65] isosurfaces reveal marked differences in electronic distribution between the orthorhombic $\text{C}222_1$ -type RE_3TaO_7 and pyrochlore $\text{RE}_2\text{Zr}_2\text{O}_7$ oxides. In both cases, yellow and blue regions around RE and O atoms indicate strong ionic character. However, the RE_3TaO_7 oxides exhibit pronounced anisotropy in charge distribution, consistent with their lower crystal symmetry and indicative of stronger local lattice distortions. In contrast, the zirconates show more isotropic and symmetric $\Delta\rho$ patterns, aligned with their higher lattice symmetry and more ordered vacancy configuration.

To quantitatively assess local structural disorder, two descriptors were defined: bond-length variance (D_b) and Bader charge variance (D_e):

$$D_b = \frac{1}{N} \sum_{i=1}^N \left(\frac{b_i - \bar{b}}{\bar{b}} \right)^2 \quad (1)$$

$$D_e = \frac{1}{N} \sum_{i=1}^N \left(\frac{e_i - \bar{e}}{\bar{e}} \right)^2 \quad (2)$$

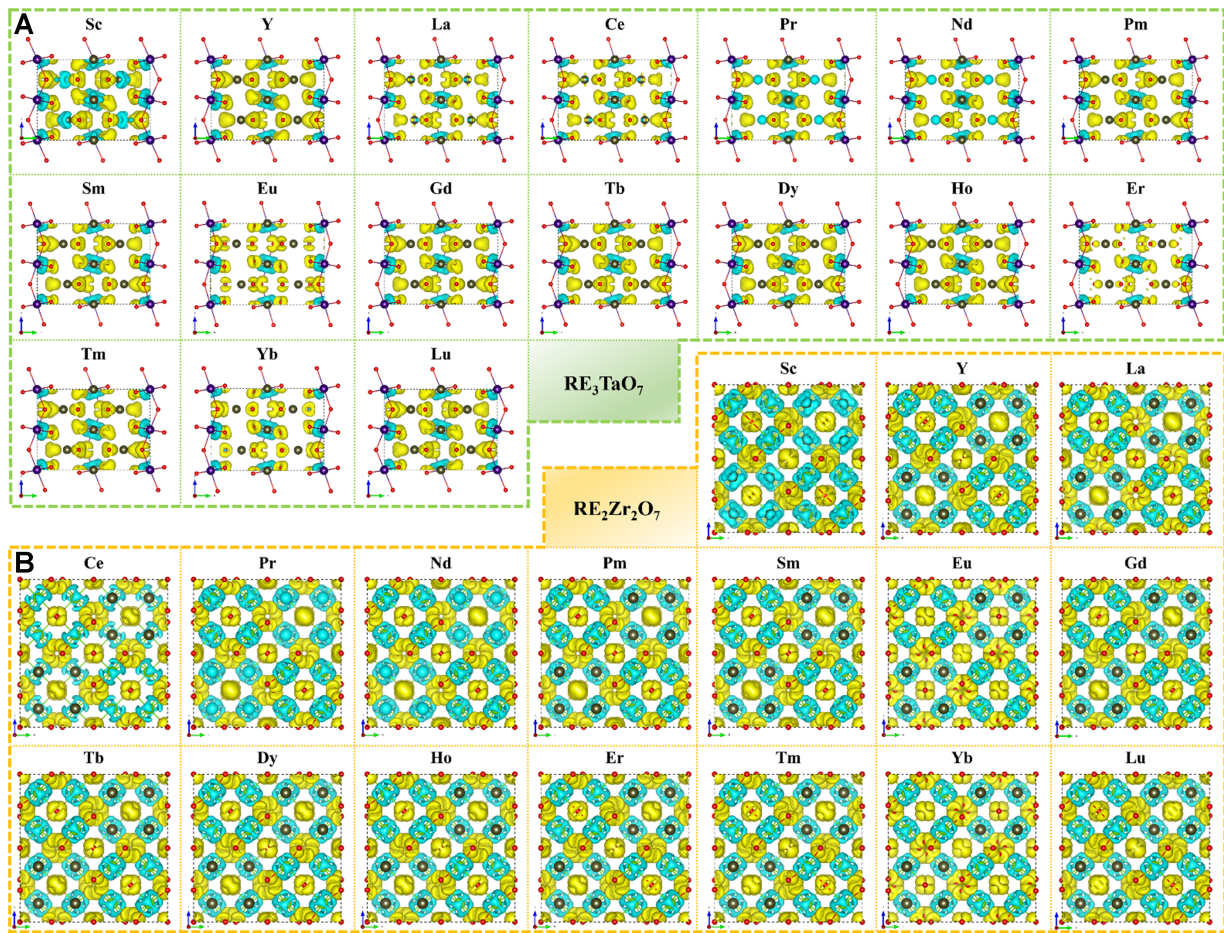


Figure 5. The bonding charge density isosurface of (A) C222₁ RE Ta₃O₇ and (B) RE₂Zr₂O₇ pyrochlore (RE = Sc, Y, La ~ Lu). The blue and yellow isosurfaces respectively correspond to $\Delta\rho \pm 0.02 \text{ e} \cdot \text{\AA}^{-3}$. RE: Rare-earth.

where b_i and e_i represent individual bond lengths and Bader charges within RE–O or Zr/Ta–O coordination environments, and \bar{b} and \bar{e} are their respective averages. N is the number of bonds or charges considered. These disorder metrics quantify fluctuations in bond distance and electronic environment, which have been linked to enhanced phonon scattering and reduced κ_L in complex oxides^[14,30].

As shown in Figure 6A, the relative bond lengths across different RE–O and Zr/Ta–O coordination units (REO₇, REO₈, and mixed REO_{7/8} polyhedra) decrease with decreasing $r_{RE^{3+}}$, reflecting the well-known lanthanide contraction. The insets illustrate representative local coordination geometries for these polyhedral units. Figure 6B presents the corresponding bond-length disorder degree D_b , which varies notably across both RE species and structural types. Materials with broader bond-length distributions, such as C222₁-type RE₃TaO₇ oxides, exhibit stronger phonon scattering and hence lower κ_L , especially at elevated temperatures^[18]. Within RE₃TaO₇ oxides, smaller RE ions tend to form shorter, stronger RE–O bonds, but the simultaneous increase in D_b moderates thermal transport by amplifying disorder-induced scattering. However, the distribution of bond lengths around the average provides a crucial descriptor related to local structural heterogeneity and strain fields within the lattice. A measure of this heterogeneity, such as the distortion degree of RE–O bond lengths, also varies across the RE series and between structures, as shown in Figure 6B. This bond length heterogeneity emerges as a significant factor influencing thermal conductivity. Materials exhibiting broader bond length distributions (higher distortion) tend to have lower κ_L particularly at high temperatures, due to enhanced phonon scattering from local disorder^[18]. For instance, the generally

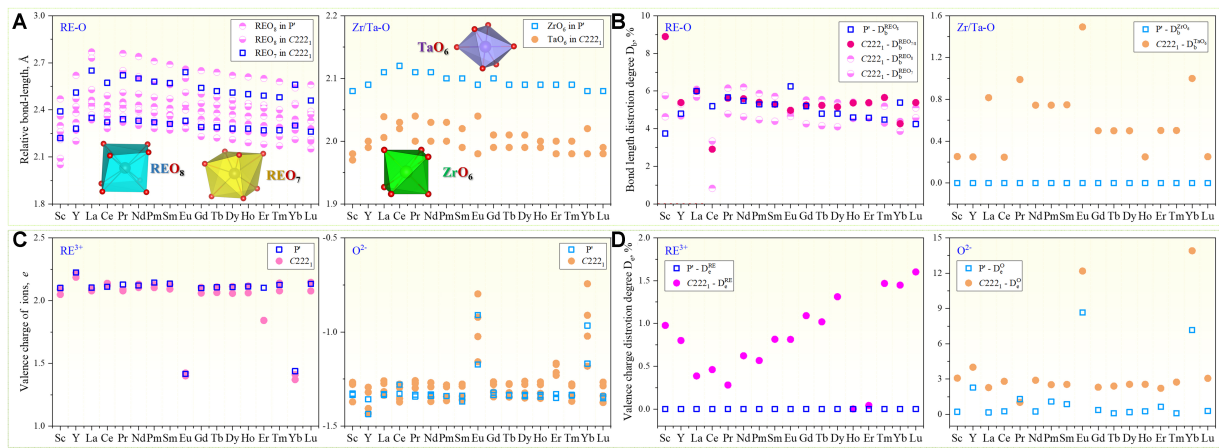


Figure 6. Bonding and charge disorder analysis in RE_3TaO_7 and $RE_2Zr_2O_7$ oxides. (A) Relative bond lengths for RE–O (left) and Zr/Ta–O (right) polyhedra, where “ REO_7 ”, “ REO_8 ” and “ $REO_{7/8}$ ” denote the 7- and 8-fold and mixed-coordination RE–O environments. Insets illustrate representative polyhedral units; (B) Bond-length disorder degree D_b of RE–O (left) and Zr/Ta–O (right) polyhedra, using the same symbol scheme as in (A); (C) Valence charges of cations RE^{3+} (left) and anions O^{2-} (right), derived from Bader charge analysis; (D) Valence charge disorder degree D_e for RE^{3+} (D_e^{RE}) and O^{2-} (D_e^{O}), quantifying charge inhomogeneity within coordination polyhedra. RE: Rare-earth.

lower κ_L of RE_3TaO_7 oxides compared to zirconates can be partly attributed to the greater structural complexity and potential for bond length variation in the lower-symmetry $C222_1$ structure. Within the RE_3TaO_7 oxides, smaller RE ions lead to shorter, stronger bonds, but the interplay with bond length heterogeneity dictates the overall κ_L . Additionally, K_{IC} is also intrinsically linked to the bonding environment. The trend of increasing K_{IC} with decreasing $r_{RE^{3+}}$ in RE_3TaO_7 oxides correlates with the formation of shorter, stronger average RE–O bonds, which increases the intrinsic resistance to bond breaking at the crack tip^[66,67], as shown in Figure 4. The generally higher toughness of pyrochlore zirconates suggests their specific ordered structure provides more effective toughening mechanisms compared to the $C222_1$ RE_3TaO_7 oxides.

In Figure 6C and D, electronic structure insights from Bader charge analysis further clarify structure–property relationships. Most RE ions exhibit Bader charges consistent with a nominal +3 oxidation state. However, Eu and Yb in the RE_3TaO_7 system show significantly lower calculated charges, indicative of a preference for the divalent (+2) state. As shown in Figure 6D, this deviation introduces local charge imbalance and strain fields, broadening the bond-length distribution and increasing D_e , which in turn destabilizes the ordered $C222_1$ structure (reflected in higher relative E_{form} , as shown in Figure 2). Interestingly, such pronounced effects are not observed in the corresponding zirconates, suggesting the more flexible fluorite-derived framework of the zirconates is better able to accommodate such charge and strain fluctuations. These mechanisms provide vital guidelines for strategically balancing K_{IC} and thermal insulation in RE-based oxide ceramics for advanced TBC applications.

Quantifying structure–property relationships

To establish direct links between atomic-scale descriptors and macroscopic thermomechanical behavior, quantitative correlation and interpretability analyses were conducted. Figure 7 presents Pearson correlation coefficient matrices and SHAP feature importance rankings for both RE_3TaO_7 and $RE_2Zr_2O_7$ oxides. The SHAP package was utilized to interpret the ML models effectively^[68]. These tools collectively identify the most influential parameters controlling κ_L and K_{IC} , including the $r_{RE^{3+}}$, V_o , E_o , E_{form} , bond energy (E_b) for RE–O, Ta–O and Zr–O bonds, and disorder metrics such as bond-length heterogeneity (D_b) and Bader charge disorder (D_e). Hierarchical clustering within the correlation matrices further highlights groups of interrelated descriptors, as visualized through dendrograms and colored sidebars.

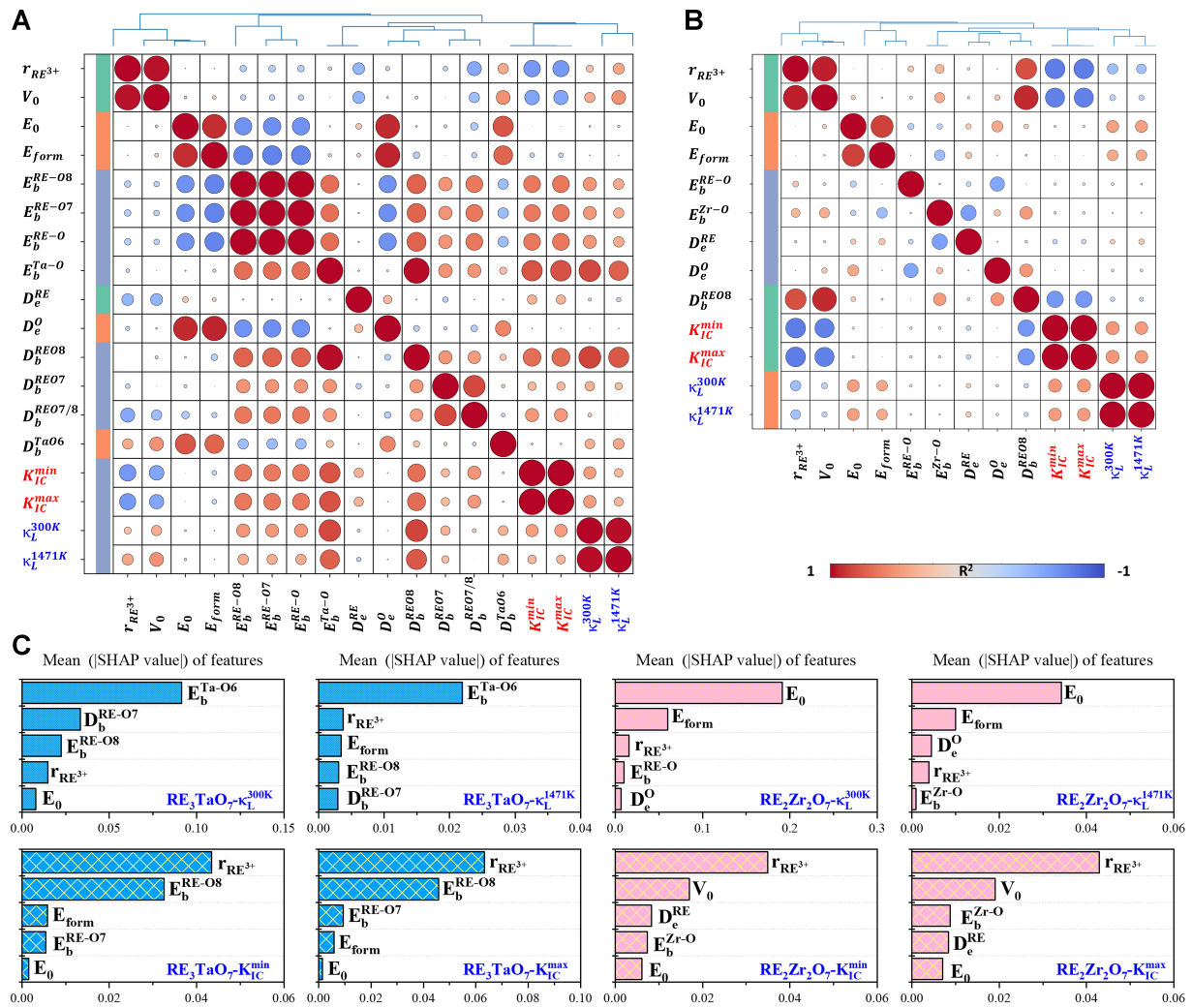


Figure 7. Correlation analysis across RE_3TaO_7 and $\text{RE}_2\text{Zr}_2\text{O}_7$ between target properties and fundamental descriptors, including are-earth ionic radius ($r_{\text{RE}^{3+}}$), equilibrium volume (V_0), total energy (E_0), formation energy (E_{form}), bond energy (E_b) for RE–O, Ta–O, and Zr–O bonds, bond-length disorder (D_b) and Bader charge disorder (D_e). Pearson correlation heatmap for (A) RE_3TaO_7 and (B) $\text{RE}_2\text{Zr}_2\text{O}_7$. Colored sidebars indicate feature clusters derived from hierarchical clustering; (C) SHAP analysis showing the top five most influential features (ranked by mean SHAP value) for predicting K_{IC} and κ_L in each system. RE: Rare-earth; SHAP: SHapley Additive exPlanations.

In RE_3TaO_7 oxides, as shown in Figure 7A, strong positive correlations are observed between $r_{\text{RE}^{3+}}$, E_0 and $E_b^{\text{RE-O}}$ with both K_{IC} and κ_L . This indicates that larger RE ions and stronger RE–O bonding contribute to enhanced structural rigidity and thermal transport capacity. Conversely, descriptors capturing local lattice disorder, such as bond-length heterogeneity ($D_b^{\text{REO7/8}}$) and RE-site Bader charge disorder (D_e^{RE}), also show positive correlation with K_{IC} , suggesting that structural distortion aids crack resistance by disrupting crack propagation pathways. Interestingly, Ta–O E_b ($E_b^{\text{Ta-O}}$) and its associated disorder (D_b^{TaO6}) display inverse correlations with κ_L , indicating that stronger, more heterogeneous Ta–O interactions exacerbate phonon scattering, thereby suppressing thermal conductivity. These findings reinforce the dual role of bonding strength and disorder in tailoring functional performance. As shown in Figure 7B, the $\text{RE}_2\text{Zr}_2\text{O}_7$ pyrochlore oxides exhibit similar, though somewhat attenuated, correlation patterns. This attenuation is attributed to their higher symmetry and reduced chemical complexity. Nevertheless, key descriptors such as Zr–O E_b ($E_b^{\text{Zr-O}}$), RE Bader charge disorder (D_e^{RE}) and RE–O bond-length disorder (D_b^{REO8}) remain strongly correlated with both K_{IC} and κ_L , confirming their general importance across systems.

To further quantify the relative importance of these descriptors, SHAP analysis was applied to trained regression models for each oxide family, as shown in Figure 7C. For RE_3TaO_7 , dominant predictive features include RE–O E_b , bond-length disorder (D_b), and E_{form} - consistent with the physical picture of configurational complexity and bond robustness as key regulators of performance. In $\text{RE}_2\text{Zr}_2\text{O}_7$, the most influential features shift slightly to Zr–O E_b , Bader charge disorder, and V_o , emphasizing the role of atomic packing and local charge environment. Taken together, both correlation-based and model-based analyses converge on three dominant descriptors: E_b , D_b and Bader charge heterogeneity (D_c), as the primary determinants of K_{IC} and κ_L across the RE series. These interpretable, physically grounded parameters elucidate the mechanisms of phonon scattering, lattice stiffening and crack resistance. Moreover, they serve as a robust foundation for data-driven materials design. Importantly, these insights explain why RE_3TaO_7 oxides, despite exhibiting intrinsically lower thermal conductivity, maintain moderate toughness. The reinforcement of RE–O bonds and local disorder-induced energy dissipation mechanisms helps compensate for structural complexity. In contrast, $\text{RE}_2\text{Zr}_2\text{O}_7$ oxides achieve a superior balance of high fracture resistance and moderate κ_L , attributable to their chemically ordered and structurally accommodating lattice framework.

CONCLUSIONS

In this work, a comprehensive data-driven framework was employed to investigate the thermomechanical performance of RE_3TaO_7 and $\text{RE}_2\text{Zr}_2\text{O}_7$ oxides, aiming to guide the rational design of advanced TBC materials. First-principles calculations and model-based analyses were used to evaluate their structural stability, thermal conductivity, and intrinsic K_{IC} across the RE series. The results reveal that RE_3TaO_7 exhibits consistently lower κ_L than $\text{RE}_2\text{Zr}_2\text{O}_7$, primarily due to its lower crystallographic symmetry, heavier atomic constituents, and higher degree of structural disorder. In contrast, $\text{RE}_2\text{Zr}_2\text{O}_7$ displays slightly higher intrinsic K_{IC} , which is attributed to its ordered vacancy sublattice and more symmetric bonding environment. However, this theoretical trend differs from experimental observations, where RE_3TaO_7 ceramics often demonstrate comparable or higher K_{IC} , likely due to extrinsic microstructural effects such as porosity, residual stress, and grain boundary interactions, which are not captured in idealized simulations. To uncover the underlying structure–property relationships, both Pearson correlation and SHAP analyses were conducted, highlighting E_b , charge disorder and bond-length heterogeneity as the most influential descriptors governing κ_L and K_{IC} . These insights not only reconcile theoretical predictions with experimental data but also provide a predictive framework for identifying and optimizing RE oxide compositions with balanced mechanical integrity and thermal insulation performance for high-temperature applications.

DECLARATIONS

Acknowledgments

This work was financially supported by the National Defense Basic Scientific Research Program (Grant Nos. 211-CXCY-N103-03-04-00 and 2022-JCKY-JJ-1086) and the National Natural Science Foundation of China (Grant No. 52204343). First-principles calculations were performed on the clusters at Northwestern Polytechnical University.

Authors' contributions

Writing - original draft preparation, conceptualization, methodology, data curation, investigation, formal analysis: Zhang, Y.

Writing - original draft preparation, supervision, methodology, editing, validation, project administration, funding acquisition: Wang, W. Y.

Data curation, investigation, formal analysis, writing - original draft preparation: Wang, Y.; Ren, K.; Wang, Z.

Conceptualization, methodology, editing, project administration: Zhang, K.

Supervision, conceptualization, methodology, editing, project administration: Gao, X.; Song, H.

Supervision, conceptualization, methodology, editing, project administration, funding acquisition: Liang, X.; Li, J.

All authors have read and agreed to the published version of the manuscript.

Availability of data and materials

Data sharing is not applicable to this article as no datasets were generated or analyzed during the current study.

Financial support and sponsorship

This work was financially supported by the National Defense Basic Scientific Research Program (Grant Nos. 211-CXCY-N103-03-04-00 and 2022-JCKY-JJ-1086).

Conflicts of interest

Wang, W. Y. is an Editor in the Junior Editorial Board of *Journal of Materials Informatics*. Wang, W. Y. was not involved in any steps of the editorial process, notably including the selection of reviewers, manuscript handling, or decision-making. The other authors declare that there are no conflicts of interest.

Ethical approval and consent to participate

Not applicable.

Consent for publication

Not applicable.

Copyright

© The Author(s) 2026.

REFERENCES

- Clarke, D. R. Materials selection guidelines for low thermal conductivity thermal barrier coatings. *Surf. Coat. Technol.* **2003**, *163*-4, 67-74. [DOI](#)
- Padture, N. P.; Gell, M.; Jordan, E. H. Thermal barrier coatings for gas-turbine engine applications. *Science* **2002**, *296*, 280-4. [DOI](#) [PubMed](#)
- Ashofteh, A.; Rajabzadeh, M. Advances in thermal barrier coatings modeling, simulation, and analysis: a review. *J. Eur. Ceram. Soc.* **2024**, *44*, 116693. [DOI](#)
- Kumar, V.; Balasubramanian, K. Progress update on failure mechanisms of advanced thermal barrier coatings: a review. *Prog. Org. Coat.* **2016**, *90*, 54-82. [DOI](#)
- Clarke, D. R.; Phillpot, S. R. Thermal barrier coating materials. *Mater. Today*. **2005**, *8*, 22-9. [DOI](#)
- Song, D.; Ryu, M.; Kwon, J.; et al. Blocking of radiative thermal conduction in Zn²⁺-incorporated high-entropy A₂B₂O₇ fluorite oxides. *Ceram. Int.* **2021**, *47*, 33544-53. [DOI](#)
- Schelling, P. K.; Phillpot, S. R.; Wolf, D. Mechanism of the cubic-to-tetragonal phase transition in zirconia and yttria-stabilized zirconia by molecular-dynamics simulation. *J. Am. Ceram. Soc.* **2001**, *84*, 1609-19. [DOI](#)
- Xiang, H.; Xing, Y.; Dai, F.; et al. High-entropy ceramics: present status, challenges, and a look forward. *J. Adv. Ceram.* **2021**, *10*, 385-441. [DOI](#)
- Wu, S.; Zhao, Y.; Li, W.; Liu, W.; Wu, Y.; Liu, F. Research progresses on ceramic materials of thermal barrier coatings on gas turbine. *Coatings* **2021**, *11*, 79. [DOI](#)
- Chen, L.; Hu, M.; Wang, J.; Li, B.; Feng, J. Dominant mechanisms of thermo-mechanical properties of weberite-type RE₃TaO₇ (RE = La, Pr, Nd, Eu, Gd, Dy) tantalates toward multifunctional thermal/environmental barrier coating applications. *Acta. Mater.* **2024**, *270*, 119857. [DOI](#)
- Chen, L.; Li, B.; Feng, J. Rare-earth tantalates for next-generation thermal barrier coatings. *Prog. Mater. Sci.* **2024**, *144*, 101265. [DOI](#)
- Haoming, Z.; Hongsong, Z.; Xiaoqin, G.; et al. Phase compositions and thermophysical performances for (Sm_{1-x}Yb_x)₃TaO₇ compounds. *Cerams. Int.* **2024**, *50*, 18576-83. [DOI](#)
- Riffe, W. T.; Zare, S.; Ardrey, K. D.; et al. Broadband optical phonon scattering reduces the thermal conductivity of multi-cation oxides. *Nat. Commun.* **2025**, *16*, 3333. [DOI](#) [PubMed](#) [PMC](#)
- Jia, H.; Li, C.; Chen, G.; Gong, B.; An, L.; Chen, K. Thermodynamic calculation, preparation and properties of Y₂(Zr_{1/6}Ti_{1/3}Ge_{1/6}Hf_{1/12}Sn_{1/4})₂O₇ high-entropy pyrochlore ceramics. *Ceram. Int.* **2024**, *50*, 22671-8. [DOI](#)

-
15. Wei, M.; Xu, J.; Zhu, J.; et al. Influence of size disorder parameter on the thermophysical properties of rare-earth-zirconate medium-entropy ceramics. *J. Am. Ceram. Soc.* **2023**, *106*, 2037–48. [DOI](#)
 16. Wan, C.; Qu, Z.; Du, A.; Pan, W. Order–disorder transition and unconventional thermal conductivities of the $(\text{Sm}_{1-x}\text{Yb}_x)_2\text{Zr}_2\text{O}_7$ series. *J. Am. Ceram. Soc.* **2011**, *94*, 592–6. [DOI](#)
 17. Ren, S.; Zong, H. X.; Tao, X. F.; et al. Boson-peak-like anomaly caused by transverse phonon softening in strain glass. *Nat. Commun.* **2021**, *12*, 5755. [DOI](#) [PubMed](#) [PMC](#)
 18. Wright, A. J.; Wang, Q.; Hu, C.; Yeh, Y.; Chen, R.; Luo, J. Single-phase duodenary high-entropy fluorite/pyrochlore oxides with an order-disorder transition. *Acta. Mater.* **2021**, *211*, 116858. [DOI](#)
 19. Teng, Z.; Tan, Y.; Zeng, S.; et al. Preparation and phase evolution of high-entropy oxides $\text{A}_2\text{B}_2\text{O}_7$ with multiple elements at A and B sites. *J. Eur. Ceram. Soc.* **2021**, *41*, 3614–20. [DOI](#)
 20. Ren, G.; Zhang, H.; Che, J.; et al. Oxygen ion diffusion in RE_3TaO_7 : why long-range migration of O^{2-} is prohibited in the defective-fluorite structure? *Acta. Mater.* **2024**, *281*, 120362. [DOI](#)
 21. Wright, A. J.; Wang, Q.; Ko, S.; Chung, K. M.; Chen, R.; Luo, J. Size disorder as a descriptor for predicting reduced thermal conductivity in medium- and high-entropy pyrochlore oxides. *Scr. Mater.* **2020**, *181*, 76–81. [DOI](#)
 22. Toher, C.; Oses, C.; Esters, M.; et al. High-entropy ceramics: propelling applications through disorder. *MRS. Bull.* **2022**, *47*, 194–202. [DOI](#)
 23. Han, Y.; Liu, X.; Zhang, Q.; et al. Ultra-dense dislocations stabilized in high entropy oxide ceramics. *Nat. Commun.* **2022**, *13*, 2871. [DOI](#) [PubMed](#) [PMC](#)
 24. Yang, Y.; Song, Z.; Lu, G.; et al. Intrinsic toughening and stable crack propagation in hexagonal boron nitride. *Nature* **2021**, *594*, 57–61. [DOI](#) [PubMed](#)
 25. Lee, S.; Esfarjani, K.; Luo, T.; Zhou, J.; Tian, Z.; Chen, G. Resonant bonding leads to low lattice thermal conductivity. *Nat. Commun.* **2014**, *5*, 3525. [DOI](#) [PubMed](#)
 26. Singh, P.; Vela, B.; Ouyang, G.; et al. A ductility metric for refractory-based multi-principal-element alloys. *Acta. Mater.* **2023**, *257*, 119104. [DOI](#)
 27. Zhang, Y.; Ren, K.; Wang, W. Y.; et al. Discovering the ultralow thermal conductive $\text{A}_2\text{B}_2\text{O}_7$ -type high-entropy oxides through the hybrid knowledge-assisted data-driven machine learning. *J. Mater. Sci. Technol.* **2024**, *168*, 131–42. [DOI](#)
 28. Gu, H.; Rohmer, J.; Jetter, J.; et al. Exploding and weeping ceramics. *Nature* **2021**, *599*, 416–20. [DOI](#) [PubMed](#)
 29. Braun, J. L.; Rost, C. M.; Lim, M.; et al. Charge-induced disorder controls the thermal conductivity of entropy-stabilized oxides. *Adv. Mater.* **2018**, *30*, e1805004. [DOI](#) [PubMed](#) [PMC](#)
 30. Sarkar, A.; Wang, Q.; Schiele, A.; et al. High-entropy oxides: fundamental aspects and electrochemical properties. *Adv. Mater.* **2019**, *31*, e1806236. [DOI](#) [PubMed](#)
 31. He, J.; Xia, Y.; Lin, W.; et al. Accelerated discovery and design of ultralow lattice thermal conductivity materials using chemical bonding principles. *Adv. Funct. Mater.* **2022**, *32*, 2108532. [DOI](#)
 32. Ritchie, R. O. The conflicts between strength and toughness. *Nat. Mater.* **2011**, *10*, 817–22. [DOI](#) [PubMed](#)
 33. Sun, C.; Huang, Y.; Shen, Q.; et al. Embedding two-dimensional graphene array in ceramic matrix. *Sci. Adv.* **2020**, *6*, eabb1338. [DOI](#) [PubMed](#) [PMC](#)
 34. Ritchie, R. O. Toughening materials: enhancing resistance to fracture. *Philos. Trans. A. Math. Phys. Eng. Sci.* **2021**, *379*, 20200437. [DOI](#) [PubMed](#)
 35. Porz, L.; Klomp, A. J.; Fang, X.; et al. Dislocation-toughened ceramics. *Mater. Horiz.* **2021**, *8*, 1528–37. [DOI](#) [PubMed](#)
 36. Han, J.; Kim, I.; Cho, N.; et al. Toward accurate machine learning-driven prediction of polymeric composites properties based on experimental data. *MGE. Adv.* **2025**, *3*, e70027. [DOI](#)
 37. Wang, W. Y.; Zhang, S.; Li, G.; et al. Artificial intelligence enabled smart design and manufacturing of advanced materials: the endless frontier in AI+ era. *MGE. Adv.* **2024**, *2*, e56. [DOI](#)
 38. Shang, Y.; Xiong, Z.; An, K.; Hauch, J. A.; Brabec, C. J.; Li, N. Materials genome engineering accelerates the research and development of organic and perovskite photovoltaics. *MGE. Adv.* **2024**, *2*, e28. [DOI](#)
 39. Wang, W. Y.; Yin, J.; Chai, Z.; et al. Big data-assisted digital twins for the smart design and manufacturing of advanced materials: from atoms to products. *J. Mater. Inf.* **2022**, *2*, 1. [DOI](#)
 40. Gao, X.; Wang, W. Y.; Chen, X.; et al. ProME: an integrated computational platform for material properties at extremes and its application in multicomponent alloy design. *MGE. Adv.* **2025**, *3*, e70029. [DOI](#)
 41. Divilov, S.; Eckert, H.; Hicks, D.; et al. Disordered enthalpy-entropy descriptor for high-entropy ceramics discovery. *Nature* **2024**, *625*, 66–73. [DOI](#) [PubMed](#) [PMC](#)

42. Xu, D.; Zhang, Q.; Huo, X.; Wang, Y.; Yang, M. Advances in data-assisted high-throughput computations for material design. *MGE. Adv.* **2023**, *1*, e11. [DOI](#)
43. Zhang, S.; Wang, W. Y.; Wang, X.; et al. Large language models enabled intelligent microstructure optimization and defects classification of welded titanium alloys. *J. Mater. Inf.* **2024**, *4*, 34. [DOI](#)
44. Carrete, J.; Li, W.; Mingo, N.; Wang, S.; Curtarolo, S. Finding unprecedentedly low-thermal-conductivity half-heusler semiconductors via high-throughput materials modeling. *Phys. Rev. X* **2014**, *4*, 011019. [DOI](#)
45. Li, Y.; Kowalski, P. M.; Beridze, G.; Birnie, A. R.; Finkeldei, S.; Bosbach, D. Defect formation energies in $A_2B_2O_7$ pyrochlores. *Scr. Mater.* **2015**, *107*, 18–21. [DOI](#)
46. Wang, Y.; Perdew, J. P. Correlation hole of the spin-polarized electron gas, with exact small-wave-vector and high-density scaling. *Phys. Rev. B. Condens. Matter.* **1991**, *44*, 13298–307. [DOI](#) [PubMed](#)
47. Amari, S.; Daoud, S. Structural phase transition, elastic constants and thermodynamic properties of TmAs: a DFT study. *Comput. Condens. Matter.* **2022**, *33*, e00764. [DOI](#)
48. Söderlind, P.; Turchi, P. E.; Landa, A.; Lordi, V. Ground-state properties of rare-earth metals: an evaluation of density-functional theory. *J. Phys. Condens. Matter.* **2014**, *26*, 416001. [DOI](#) [PubMed](#)
49. Loschen, C.; Carrasco, J.; Neyman, K. M.; Illas, F. First-principles LDA+U and GGA+U study of cerium oxides: dependence on the effective U parameter. *Phys. Rev. B.* **2007**, *75*, 035115. [DOI](#)
50. Singh, P.; Del Rose, T.; Vazquez, G.; Arroyave, R.; Mudryk, Y. Machine-learning enabled thermodynamic model for the design of new rare-earth compounds. *Acta. Mater.* **2022**, *229*, 117759. [DOI](#)
51. Birch, F. Finite elastic strain of cubic crystals. *Phys. Rev.* **1947**, *71*, 809–24. [DOI](#)
52. Chung, D. H.; Buessem, W. R. The Voigt-Reuss-Hill approximation and elastic moduli of polycrystalline MgO, CaF_2 , β -ZnS, ZnSe, and CdTe. *J. Appl. Phys.* **1967**, *38*, 2535–40. [DOI](#)
53. Hill, R. The elastic behaviour of a crystalline aggregate. *Proc. Phys. Soc. A.* **1952**, *65*, 349–54. [DOI](#)
54. Wan, C.; Zhang, W.; Wang, Y.; et al. Glass-like thermal conductivity in ytterbium-doped lanthanum zirconate pyrochlore. *Acta. Mater.* **2010**, *58*, 6166–72. [DOI](#)
55. To, T.; Sørensen, S. S.; Stepniowska, M.; et al. Fracture toughness of a metal-organic framework glass. *Nat. Commun.* **2020**, *11*, 2593. [DOI](#) [PubMed](#) [PMC](#)
56. Griffith, A. A. VI. The phenomena of rupture and flow in solids. *Philos. Trans. A. Math. Phys. Eng. Sci.* **1921**, *221*, 163–98. [DOI](#)
57. Zhang, Y.; Wang, W. Y.; Li, P.; et al. Hook's law scaled broken-bond model for surface energy: from metals to ceramics. *Scr. Mater.* **2024**, *244*, 116026. [DOI](#)
58. Niu, H.; Niu, S.; Oganov, A. R. Simple and accurate model of fracture toughness of solids. *J. Appl. Phys.* **2019**, *125*, 065105. [DOI](#)
59. Mazhnik, E.; Oganov, A. R. A model of hardness and fracture toughness of solids. *J. Appl. Phys.* **2019**, *126*, 125109. [DOI](#)
60. Wang, J.; Zhang, F.; Lian, J.; Ewing, R. C.; Becker, U. Energetics and concentration of defects in $Gd_2Ti_2O_7$ and $Gd_2Zr_2O_7$ pyrochlore at high pressure. *Acta. Mater.* **2011**, *59*, 1607–18. [DOI](#)
61. Shamblin, J.; Tracy, C. L.; Palomares, R. I.; et al. Similar local order in disordered fluorite and aperiodic pyrochlore structures. *Acta. Mater.* **2018**, *144*, 60–7. [DOI](#)
62. Zhang, Y.; Ren, K.; Wang, W. Y.; et al. Smart design $A_2Zr_2O_7$ -type high-entropy oxides through lattice-engineering toughening strategy. *npj. Comput. Mater.* **2024**, *10*, 1462. [DOI](#)
63. Yokogawa, Y.; Yoshimura, M. Formation and stability regions of the high-temperature fluorite-related phase in the R_2O_3 - Ta_2O_5 system ($R = La, Nd, Sm, Ho, Er$, and Yb). *J. Am. Ceram. Soc.* **1997**, *80*, 1965–74. [DOI](#)
64. Labrincha, J. A.; Frade, J. R.; Marques, F. M. B. $La_2Zr_2O_7$ formed at ceramic electrode/YSZ contacts. *J. Mater. Sci.* **1993**, *28*, 3809–15. [DOI](#)
65. Su, L.; Huyan, H.; Sarkar, A.; et al. Direct observation of elemental fluctuation and oxygen octahedral distortion-dependent charge distribution in high entropy oxides. *Nat. Commun.* **2022**, *13*, 2358. [DOI](#) [PubMed](#) [PMC](#)
66. Cui, K.; Sun, T. L.; Liang, X.; et al. Multiscale energy dissipation mechanism in tough and self-healing hydrogels. *Phys. Rev. Lett.* **2018**, *121*, 185501. [DOI](#)
67. Cui, K.; Ye, Y. N.; Sun, T. L.; et al. Effect of structure heterogeneity on mechanical performance of physical polyampholytes hydrogels. *Macromolecules* **2019**, *52*, 7369–78. [DOI](#)
68. Roth, A. E. Lloyd Shapley (1923–2016). *Nature* **2016**, *532*, 178. [DOI](#) [PubMed](#)
69. Zhao, X.; Guo, L.; Wang, C.; Zhang, Y.; Ye, F. Effect of phase structure evolution on thermal expansion and toughness of $(Nd_{1-x}Sc_x)_2Zr_2O_7$ ($x = 0, 0.025, 0.05, 0.075, 0.1$) ceramics. *J. Mater. Sci. Technol.* **2017**, *33*, 192–7. [DOI](#)
70. Hua, Y.; Jiang, B.; Chen, R.; Cao, J.; Shuai, W.; Li, R. Enhanced physical properties of $TiSi_2$ doped $Gd_2Zr_2O_7$ ceramic for thermal barrier coatings. *Mater. Res. Express.* **2019**, *6*, 056547. [DOI](#)

71. Wang, C.; Guo, L.; Zhang, Y.; Zhao, X.; Ye, F. Enhanced thermal expansion and fracture toughness of Sc_2O_3 -doped $\text{Gd}_2\text{Zr}_2\text{O}_7$ ceramics. *Ceram. Int.* **2015**, *41*, 10730–5. DOI
72. Tu, T.; Liu, J.; Zhou, L.; Liang, Y.; Zhang, G. Graceful behavior during CMAS corrosion of a high-entropy rare-earth zirconate for thermal barrier coating material. *J. Eur. Ceram. Soc.* **2022**, *42*, 649–57. DOI
73. Liu, D.; Shi, B.; Geng, L.; Wang, Y.; Xu, B.; Chen, Y. High-entropy rare-earth zirconate ceramics with low thermal conductivity for advanced thermal-barrier coatings. *J. Adv. Ceram.* **2022**, *11*, 961–73. DOI
74. Mao, W.; Wang, Y.; Huang, H.; et al. In situ characterizations of mechanical behaviors of freestanding $(\text{Gd}_{0.9}\text{Yb}_{0.1})_2\text{Zr}_2\text{O}_7$ coatings by bending tests under different temperatures based on digital image correlation. *J. Eur. Ceram. Soc.* **2020**, *40*, 491–502. DOI
75. Wang, D.; Dong, S.; Zeng, J.; et al. Influence of doping Mg^{2+} or Ti^{4+} captions on the microstructures, thermal radiation and thermal cycling behavior of plasma-sprayed $\text{Gd}_2\text{Zr}_2\text{O}_7$ coatings. *Ceram. Int.* **2020**, *46*, 13054–65. DOI
76. Ren, X.; Wan, C.; Zhao, M.; Yang, J.; Pan, W. Mechanical and thermal properties of fine-grained quasi-eutectoid $(\text{La}_{1-x}\text{Yb}_x)_2\text{Zr}_2\text{O}_7$ ceramics. *J. Eur. Ceram. Soc.* **2015**, *35*, 3145–54. DOI
77. Yan, R.; Liang, W.; Miao, Q.; et al. Mechanical, thermal and CMAS resistance properties of high-entropy $(\text{Gd}_{0.2}\text{Y}_{0.2}\text{Er}_{0.2}\text{Tm}_{0.2}\text{Yb}_{0.2})_2\text{Zr}_2\text{O}_7$ ceramics. *Ceram. Int.* **2023**, *49*, 20729–41. DOI
78. Ren, K.; Wang, Q.; Shao, G.; Zhao, X.; Wang, Y. Multicomponent high-entropy zirconates with comprehensive properties for advanced thermal barrier coating. *Scr. Mater.* **2020**, *178*, 382–6. DOI
79. Guo, L.; Zhang, Y.; Zhao, X.; Wang, C.; Ye, F. Thermal expansion and fracture toughness of $(\text{RE}_{0.9}\text{Sc}_{0.1})_2\text{Zr}_2\text{O}_7$ (RE = La, Sm, Dy, Er) ceramics. *Ceram. Int.* **2016**, *42*, 583–8. DOI
80. Zhang, Y.; Guo, L.; Zhao, X.; Wang, C.; Ye, F. Toughening effect of Yb_2O_3 stabilized ZrO_2 doped in $\text{Gd}_2\text{Zr}_2\text{O}_7$ ceramic for thermal barrier coatings. *Mater. Sci. Eng. A.* **2015**, *648*, 385–91. DOI
81. Guo, L.; Guo, H.; Peng, H.; Gong, S. Thermophysical properties of Yb_2O_3 doped $\text{Gd}_2\text{Zr}_2\text{O}_7$ and thermal cycling durability of $(\text{Gd}_{0.9}\text{Yb}_{0.1})_2\text{Zr}_2\text{O}_7/\text{YSZ}$ thermal barrier coatings. *J. Eur. Ceram. Soc.* **2014**, *34*, 1255–63. DOI
82. Wu, Y.; Zheng, L.; He, W.; He, J.; Guo, H. Effects of Yb^{3+} doping on phase structure, thermal conductivity and fracture toughness of $(\text{Nd}_{1-x}\text{Yb}_x)_2\text{Zr}_2\text{O}_7$. *Ceram. Int.* **2019**, *45*, 3133–9. DOI
83. Chen, L.; Hu, M.; Wu, F.; Song, P.; Feng, J. Thermo-mechanical properties of fluorite Yb_3TaO_7 and Yb_3NbO_7 ceramics with glass-like thermal conductivity. *J. Alloys. Compd.* **2019**, *788*, 1231–9. DOI

Disclaimer/Publisher's Note: All statements, opinions, and data contained in this publication are solely those of the individual author(s) and contributor(s) and do not necessarily reflect those of OAE and/or the editor(s). OAE and/or the editor(s) disclaim any responsibility for harm to persons or property resulting from the use of any ideas, methods, instructions, or products mentioned in the content.



© The Author(s) 2026. Open Access This article is licensed under a Creative Commons Attribution 4.0 International License (<https://creativecommons.org/licenses/by/4.0/>), which permits unrestricted use, sharing, adaptation, distribution and reproduction in any medium or format, for any purpose, even commercially, as long as you give appropriate credit to the original author(s) and the source, provide a link to the Creative Commons license, and indicate if changes were made.